Reports on Geodesy and Geoinformatics, 2025, Vol. 119, pp. 99–108

DOI: 10.2478/rgg-2025-0010
Received: 13 December 2024 / Accepted: 25 April 2025
Published online: 19 May 2025

ORIGINAL ARTICLE

A modified Distributed Scatterer InSAR method: A case study on potential landslide body detection in Faer Town, China

Zhibao Nie [1*], Mintao Ding [1], Shijun Ding [1], Xvli Wang [2], Keru Jiang [2] and Jinfeng Zhang [3]

[1]Geotechnical Engineering Laboratory, China Electric Power Research Institute, Beijing, 100192, China
[2]State Grid Economic and Technology Research Institute of Anhui Electric Power Co., Ltd., Hefei 230006, China
[3]State Grid Anhui Electric Power Co., Ltd., Hefei 230061, China

[*]hndlsjy20241017@163.com

Abstract

Landslides near critical infrastructure, such as power transmission lines, represent significant safety and economic risks, especially in regions prone to geohazards. Early detection and monitoring are essential to mitigate potential damage. Interferometric Synthetic Aperture Radar (InSAR) technology has become a powerful tool for detecting slow-moving landslides and monitoring millimetre-scale ground displacements over time. Among the various satellite data sources, Sentinel-1 provides consistent and high-resolution data, advancing research in landslide kinematics and instability prediction. However, accurate delineation of landslide-affected areas remains particularly challenging in densely vegetated regions, where signal decorrelation limits traditional methods. To address these limitations, this study introduces a modified Distributed Scatterer InSAR (DSI) method designed to assess landslide velocity more effectively. The proposed approach incorporates a regularization technique into the covariance matrix estimation process, reducing phase estimation bias and improving the signal-to-noise ratio of displacement time series. The modified DSI method was applied to the Faer Town landslide in Guizhou Province, Southwest China. Results from synthetic and real-data experiments demonstrate significant improvements in the accuracy and reliability of landslide velocity detection, with a higher density of reliable measurement points compared to traditional approaches. These findings highlight the method's potential for enhancing landslide monitoring and risk mitigation in challenging environments.

Key words: landslides, Distributed Scatterers InSAR, regularization, covariance matrix, Faer town

1 Introduction

Due to fragile geological conditions, rainfall, weathering processes, and human activities, landslides in Southwest China have caused significant damage to local residents (Jia et al., 2022; Zhou et al., 2020; Zhang et al., 2021; Dai et al., 2022). Faer Town, located in Shuicheng County, Guizhou Province, China, has been particularly affected by extensive underground coal mining activities. These activities disrupt the stress distribution of the overlying rock strata, especially in karst mountainous regions with fragile geological conditions, often leading to dangerous rockfalls or landslides (Li et al., 2022; Guo et al., 2022; Hu et al., 2018), which can cause incalculable damage to transmission lines along the path. Reports indicate that coal mining activities in Faer Town have resulted in approximately 80 landslides, affecting an area of about 2.8 million square meters (Jiao et al., 2013; Wu et al., 2023).

Previous studies on the Faer landslide have mainly focused on field surveys, numerical simulations, microseismic source location, rockfall deposition simulation, and sensitivity prediction (Jiao et al., 2013; Wu et al., 2023). However, there has been limited application of techniques for the quantitative monitoring of landslide deformation. Moreover, past research has primarily concentrated on landslides that have already occurred, leaving the movement processes of potentially unstable slopes largely unexplored. Thus, it is essential to investigate the spatial extent, temporal evolution, and potential risk zones for transmission lines impacted by the Faer landslide.

Interferometric Synthetic Aperture Radar (InSAR) technology, known for its wide coverage and high spatial and temporal resolution, has been successfully applied to landslide deformation detection and measurement (He et al., 2023a; Fobert et al., 2021; Moretto et al., 2021; van Natijne et al., 2022; Li et al., 2021; He et al., 2023b; Dai et al., 2022). Over the past two decades, multi-temporal InSAR methods based on Persistent Scatterer (PS) (Ferretti et al., 2001) or Distributed Scatterer (DS) (Ferretti et al., 2011) have been proposed to identify potential risks and retrieve deformation time series for landslides. The goal of Persistent Scatterer Interferometry (PSI) is to select stable targets and remove atmospheric phase screens and other noise to obtain accurate deformation results. A series of PSI techniques, such as Interferometric Point Target Analysis (IPTA) (Werner et al., 2003), Stanford Method for Persistent Scatterers (StaMPS) (Hooper, 2008), and Quasi-Persistent Scatterers (Perissin and Wang, 2011), have advanced the application of InSAR in landslide monitoring. On the other hand, the Small Baseline Subset (SBAS) is a typical method for DS interferometry (DSI) (Berardino et al., 2002), which mitigates decorrelation by selecting interferograms with short temporal and spatial baselines. Improved SBAS methods, such as Multiscale InSAR Time Series (Hetland et al., 2012), Intermittent SBAS (ISBAS) (Bateson et al., 2015), and the Python-based Miami InSAR Time Series software (MintPy) (Yunjun et al., 2019), have been developed to minimize decorrelation effects. As another framework of DSI, SqueeSAR was proposed to explore a solution using a redundant network of all possible interferograms with maximum likelihood estimation (Ferretti et al., 2011).

Despite the advancements in InSAR technology, its application for landslide monitoring in mountainous areas with dense vegetation faces significant challenges. Key limiting factors include spatiotemporal decorrelation, complex terrain, and atmospheric disturbances, all of which reduce the accuracy of InSAR measurements. These challenges are particularly pronounced in regions traversed by critical infrastructure such as transmission lines, where accurate monitoring is essential for risk mitigation. Karst landslides, common in such regions, are often covered by dense vegetation, which significantly reduces the number of persistent scatterer (PS) targets that can be reliably identified. This scarcity of PS targets results in limited deformation data, making it difficult to track landslide activity with high precision.

Additionally, the distributed scatterer (DS) method, which uses the maximum likelihood estimation criterion, often suffers from considerable computational complexity (Ansari et al., 2018). This heavy computational load complicates the establishment of robust relationships between observed deformation patterns and underlying failure mechanisms, a critical requirement for understanding landslide dynamics and predicting future behaviour.

To address these challenges, researchers have explored alternative methods to improve phase estimation accuracy in vegetated regions. For instance, eigenvalue decomposition (EVD) of the covariance matrix has been employed to estimate the optimal phase of interferograms (Fornaro et al., 2015), which enhances both the quantity and quality of coherent targets in densely vegetated areas. Other regularization strategies have also shown promise in calibrating covariance matrix magnitudes, including M-estimators, Hadamard-spectral regularization, and shrinkage techniques (Schmitt et al., 2014; Vu et al., 2023; Zhao et al., 2023; Wang and Zhu, 2016). These methods leverage the full exploitation of coherence, achieving strong performance in scenarios where long-term coherence can be maintained.

However, these approaches encounter limitations in fast-decorrelation environments, where coherence levels approach zero. In such cases, as demonstrated by recent studies, methods that rely on low-coherence interferometric pairs, while beneficial for improving phase estimation accuracy under persistent scatterer interferometry (PSI) (Ferretti et al., 2001), tend to underperform in distributed scatterer interferometry (DSI) scenarios (Ferretti et al., 2011). The loss of coherence in rapidly decorrelating landscapes, such as those affected by vegetation and topographic complexity, severely hampers the reliability of phase measurements and the accuracy of deformation time series.

In this study, we introduce a novel regularization method into the Distributed Scatterer InSAR technique, leveraging C-band Sentinel-1 data to overcome the limitations posed by dense vegetation and complex terrain. This method is applied to detect potentially unstable slopes in the Faer landslide, a region characterized by high landslide risk due to both natural and anthropogenic factors. The remainder of this paper is organized as follows: first, we introduced the study area, and the SAR dataset used in the analysis, followed by a detailed explanation of the methodological framework. We then presented and discussed the results, highlighting the method's effectiveness in identifying landslide deformation. Finally, we summarized the key findings and discussed the implications for future landslide monitoring efforts.

2 Materials and methods

2.1 Study region and datasets

The Faer landslide, located in Shuicheng County, China, occurred in a region of rugged terrain influenced by tectonic erosion and underground mining. This region, characterized by multiple active landslides along the Beipan River slopes, recently experienced a significant landslide in Jichangzhen on 23 July 2019, causing substantial human and economic losses (Dong et al., 2022). The area's subtropical monsoon climate, with abundant rainfall and dense vegetation, leads to rapid decorrelation, making it an ideal test site for landslide body detection using InSAR methods. For this study, we analysed 100 Sentinel-1 images acquired from ascending Track 128 between 4 December 2018 and 17 February 2023 (see Figure 1). SAR image co-registration was performed using a two-step strategy: first, external one-arc SRTM DEM data facilitated geometrical co-registration (Ma et al., 2020) and topographic phase removal; then, a network-based enhanced spectral diversity method (Ma et al., 2019) refined the accuracy to 0.001 pixel in the azimuth direction. Using the co-registered SLC images, we applied the sequential selection algorithm to identify DS candidates for subsequent coherence matrix and phase estimation. After phase estimation of all interferograms, we then unwrapped all interferograms (Ma et al., 2021) and converted them into the reference of the first-time acquisition. Then w could fit the velocity from the time series using a 1-order polynomial fit.

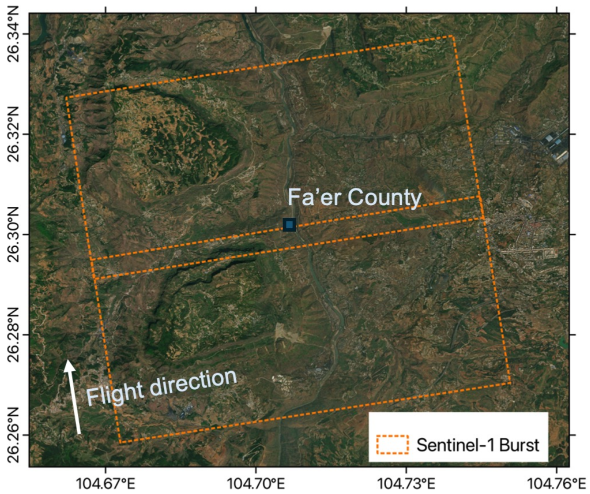

Figure 1. Satellite image of the landslide region and the used data coverage of Sentinel-1 SAR images of ascending Track 128

2.2 Modified Distributed Scatterer InSAR

Over the past decade, phase triangularity has been demonstrated as an effective constraint for improving the InSAR phase signal-to-noise ratio (SNR) (Ferretti et al., 2011). One of the most efficient phase estimators based on this approach is the Eigenvalue Maximization Interferometry (EMI) method (Ansari et al., 2018), which derives the maximum likelihood estimation (MLE) of phase solutions by minimizing the smallest eigenvector of the full covariance matrix. The mathematical formulation for a single pixel is provided by Ansari et al. (2018, 2017):

$$\hat{\Sigma} = \frac{xx^H}{n},$$
$$\hat{\Phi} = argmin_{\Phi} \left\{ \xi^H (\hat{\Upsilon}^{-1} \circ \hat{\Sigma}) \xi \right\}. \tag{1}$$

Here, $\hat{\Phi} = \angle \xi$ denotes the estimated phase series, and ξ represents the minimum eigenvector of the Hadamard product $\hat{\Upsilon}^{-1} \circ \hat{\Sigma}$, where $\hat{\Upsilon}^{-1}$ is a key factor for weighting the noise level. The superscript H indicates the Hermitian transpose. $\hat{\Sigma}$ is the estimated full covariance matrix, constructed from m SLCs and n pixels within a homogeneous region (Ferretti et al., 2011). $\hat{\Upsilon}$ is the coherence matrix, consisting of the modulus of $\hat{\Sigma}$, where each element shown below represents the coherence between two time nodes i and j,

$$\hat{\Upsilon}_{i,j} = \sum_{p \in \Omega} e^{\sqrt{-1}\left\{\angle\left(x_{i,p} x^*_{j,p}\right)\right\}}. \tag{2}$$

The theoretical probability dense function of the covariance matrix $\hat{\Sigma}$ is formed by Deledalle et al. (2015):

$$p\left(\hat{\Sigma}|\Sigma\right) = \frac{n^{nm}\left|\hat{\Sigma}\right|^{n-m}}{\Gamma_m(n)\,|\Sigma|^n} e^{-n \cdot Tr(\Sigma^{-1}\hat{\Sigma})}. \tag{3}$$

Here, Tr denotes the matrix trace, and Γ represents the hypergeometric function. When $n < m$, the covariance matrix $\hat{\Sigma}$ becomes nearly singular, as its determinant approaches zero. In this case, equation (3) is considered a degenerate distribution. Consequently, the coherence matrix $\hat{\Upsilon}$ is not of full rank, and its inverse $\hat{\Upsilon}^{-1}$ amplifies the estimation error of $\hat{\Upsilon}$, further propagating this error to the estimation of $\hat{\Phi}$.

For long time series, where m is typically large, the Sequential Estimator (Seq) method (Dong et al., 2022) can help reduce the occurrence of singularities. Seq works by dividing the full covariance matrix into several block diagonals and sequentially compressing them into rank-1 subspace clusters. Through subspace clustering, these block diagonals are connected to a unique phase datum, resulting in an estimated phase with a higher SNR than the original EMI method.

The size of the block diagonals in Seq is manually selected by the user. For example, choosing a diagonal matrix size of 20 corresponds to a 120-day time baseline. In this case, the sample pixel number only needs to be greater than 20 to reduce the occurrence of singularities. However, an unresolved issue from previous studies arises when the sample number is less than the block diagonal matrix size, leaving the question of how to improve the estimation of the precision matrix $\hat{\Upsilon}$.

To suppress matrix singularity, regularization techniques are commonly employed. A matrix can be made positive definite by either adding a small value to its diagonal or truncating small eigenvalues. However, determining the appropriate value for minimizing the estimation error of $\hat{\Upsilon}$ while maximizing the estimation accuracy of $\hat{\Phi}$ is challenging.

To address this, we propose applying a non-thresholding regularization method to Seq+EMI, aiming to further improve InSAR phase estimation accuracy. This new regularization approach conditions the coherence matrix by adding a scaled unit matrix I as:

$$\rho = \frac{\lambda(\hat{\Upsilon})_{max} - \lambda(\hat{\Upsilon})_{min} M_{max}}{M_{max} - 1}. \tag{4}$$

Here, the eigenvalue λ of the symmetric positive definite coherence matrix $\hat{\Upsilon}$ is defined as $\lambda(\hat{\Upsilon})_{max} \geq \ldots \geq \lambda(\hat{\Upsilon})_{min} > 0$, and the threshold condition number M_{max} is set between $1 \leq M_{max} \leq M$. The condition number M in the L2 norm is expressed as $M = \frac{\lambda(\hat{\Upsilon})_{max}}{\lambda(\hat{\Upsilon})_{min}}$. In this context, the reconditioned coherence matrix $\hat{\Upsilon}$ is formed by:

$$\hat{\Upsilon}_r = \hat{\Upsilon} + \rho I. \tag{5}$$

Equation (5) represents a regularization technique for least squares problems, functioning similarly to Tikhonov regularization. However, in the context of EMI, ridge regression is applied solely to recondition the coherence matrix. The regularized matrix is then inverted and used as a weighting matrix in the phase optimization process.

2.3 Phase stacking for the reliable velocity estimation

Slope instability often occurs prior to sliding events and is accompanied by significant deformation characteristics. The registration of Sentinel-1 images is based on a cross-correlation optimization algorithm, which can estimate the offsets in the slant range and azimuth directions with sub-pixel accuracy. A direct method for deriving the deformation rate from a set of unwrapped interferograms involves dividing the sum of the phases by the sum of the time intervals (Eq. 1). However, the phase stacking method weights the interferograms based on their temporal baselines, effectively suppressing atmospheric delays and random noise in the time domain. Although the average deformation rate represents only the linear deformation component over the observation period, it can serve as an indicator for identifying locations with significant surface deformation and recognizing potentially unstable areas. Therefore, this method is employed to extract the deformation rate in Faer County.

3 Results

3.1 Synthetic data test on the theoretical accuracy

In the synthetic data test, following the synthetic coherence matrix simulation described by Ansari et al. (2018); Dong et al. (2022), we used an exponential decorrelation model to simulate a coherence matrix with a constant time of 27 days, a short-term coherence of 0.6, and a long-term coherence of 0.1. To evaluate phase estimation performance, we tested various methods, as shown in Figure 2, including EMI, Seq+EMI, and the newly integrated regularization approach (Seq+EMI+reg). The tests were conducted in two scenarios: both with a time baseline of 600 days (100 SLCs), but with 49 and 121 samples for phase estimation, respectively. The homogeneous pixel number for each pixel was randomly set to either 49 or 121. We then applied the previously mentioned methods to recover all interferograms. Comparisons were made between the original phase and the phase after multilooking, EMI, Seq+EMI, and Seq+EMI+reg. The first and second rows display the estimated phase time series with a 600-day temporal baseline after applying each method but with different sample numbers. Seq+EMI, when using the regularized coherence matrix, achieves higher estimation accuracy than the original EMI and Seq+EMI. Notably, in Figure 2b, the performances of Seq+EMI and Seq+EMI+reg are close, whereas Figure 2a shows an improvement with the new estimator. This performance gain can be attributed to the improved precision matrix estimation through regularization. In Figure 2b, 121 samples were used, a number significantly larger than the stack size, ensuring that the coherence matrix remained positively definite in Seq, thus negating the need for regularization. However, with only 49 samples (Figure 2a), regularization became necessary, resulting in improved performance, as indicated by the higher phase SNR. This improvement suggests that regularization enhances the accuracy of the precision matrix, bringing it closer to the true values.

To further assess the velocity estimation performance of these methods, we simulated deformations using the "peaks" function in MATLAB. The simulated velocity map is shown in Figure 3. Using the synthetic coherence matrix, we generated 100 SAR images in SAR coordinate reference, each with a size of 200 by 800 (azimuth by range). The time-dependent deformation phase was simulated using the "peaks" function, while noise components were derived from the coherence matrix. Topographic and flat-earth phases were simulated using precise orbits and external DEM. After stacking all recovered interferograms, we obtained velocity estimates. Visual inspection of the velocity maps shows that the SNR progressively increases (with smoother fringes) from left to right. Overall, the new method demonstrates the most significant improvement, particularly after the introduction of regularization, which more points. The velocity estimation accuracy of the new estimator outperforms the other methods, as its deviation from the true value is the smallest. These comparisons confirm that SNR is a critical factor influencing velocity estimation accuracy.

3.2 Phase SNR comparison on real data

First, we visually assess the performance of various phase estimation algorithms in recovering the wrapped phase time series. We compare the original phase with the multilooked phase, EMI, Seq+EMI, and our proposed method. All phase estimation algorithms are applied at full spatial resolution without pre-multilooking, allowing a direct comparison of their effectiveness.

Figure 4 shows two reconstructed sample interferograms

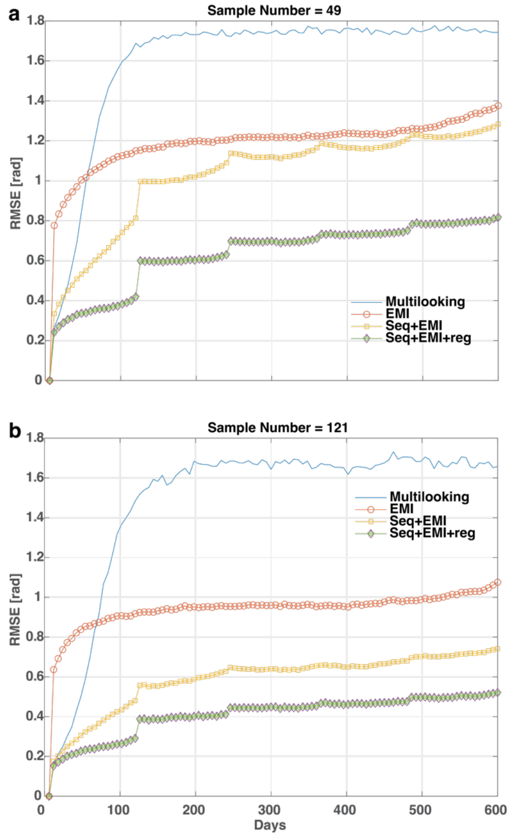

Figure 2. Theoretical accuracy (phase root mean square error) of four methods: (a) sample number 49, (b) sample number 121

with different temporal baselines. The noise level in the original phase is relatively high, even in the shortest temporal baseline interferogram (12 days). In contrast, the phase estimation methods demonstrate significant improvements in recovering the signal, as shown in Figure 2. While all methods reduce noise, the improvements are more pronounced in methods other than EMI. This is because the latter methods exclude weakly coherent pairs during temporal phase filtering, unlike EMI, which applies a full-stack approach. To further validate the results, we analysed a longer temporal baseline interferogram (84 and 168 days), shown in Figure 4. As expected, severe decorrelation noise almost entirely obscured the useful signal in Figure 4. Although the existing phase estimation methods recovered some of the interferometric phases, they remained largely ineffective in other regions. In contrast, our method consistently delivered satisfactory performance across the interferogram. We concluded that the proposed estimator is highly effective in both short- and long-term interferogram phase recovery.

To quantify the performance, we evaluated the phase quality across different phase estimators by calculating the variation in SNR before and after phase estimation. The SNR metric is defined as:

$$\mathrm{SNR} = 10\log_{10}\frac{\delta^2_{\phi}}{\delta^2_{\hat{\phi}}}, \tag{6}$$

where δ^2_{ϕ} and $\delta^2_{\hat{\phi}}$ are the original and optimized phase variances, respectively.

The phase variances for each pixel were calculated using a symmetric window with dimensions of 10×40 (azimuth by range). To ensure robust estimation of velocity, the normal-

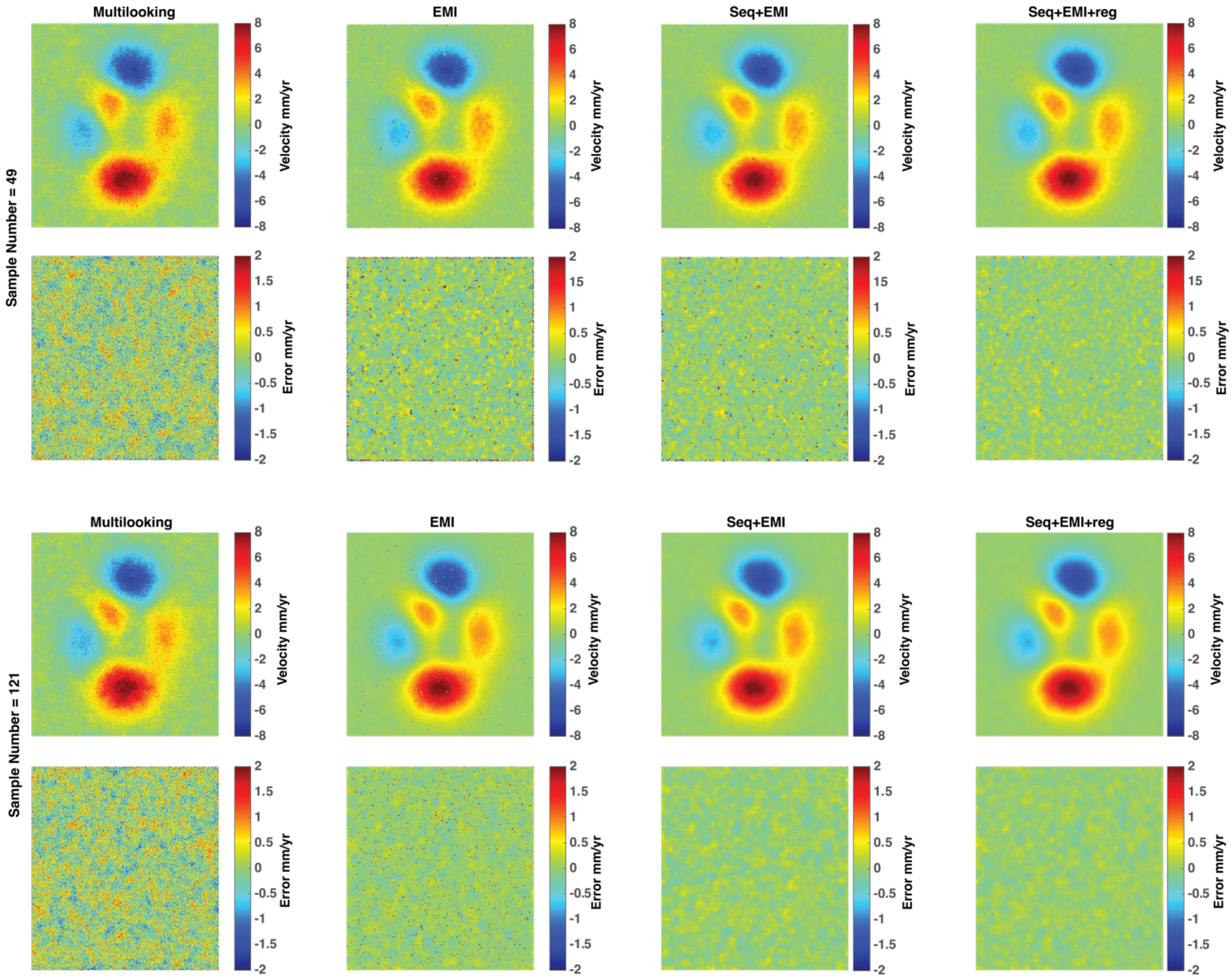

Figure 3. Estimated velocity maps with two different sample numbers. The first line represents the velocity maps estimated by four different methods, and the second line represents their errors from the true values. The third and fourth lines represent the same order, but the sample number used is different. The results of the first two lines are based on the sample number of 49 and the last two lines of 121.

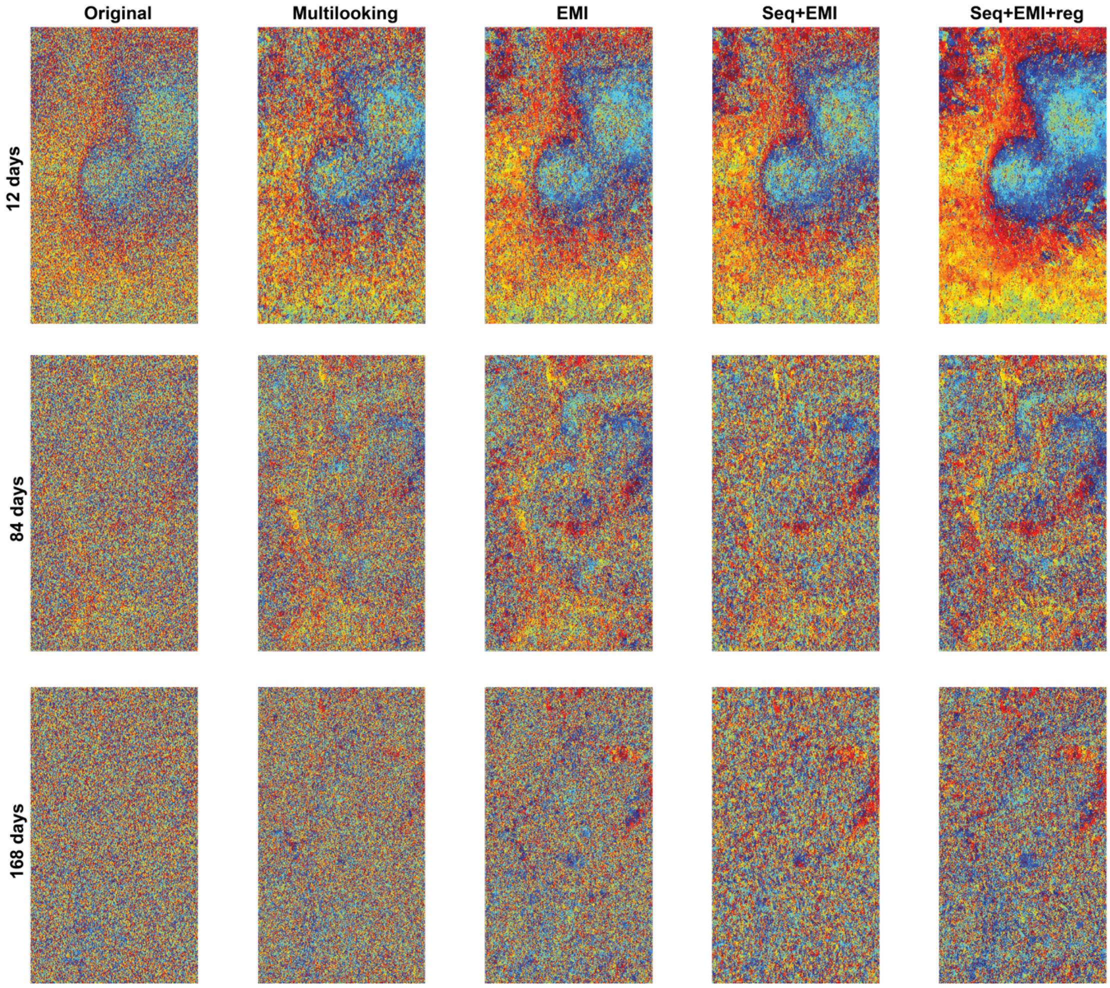

Figure 4. Estimated interferograms with three different time baselines. Each line represents a different time baseline. Each column denotes the results of the different methods.

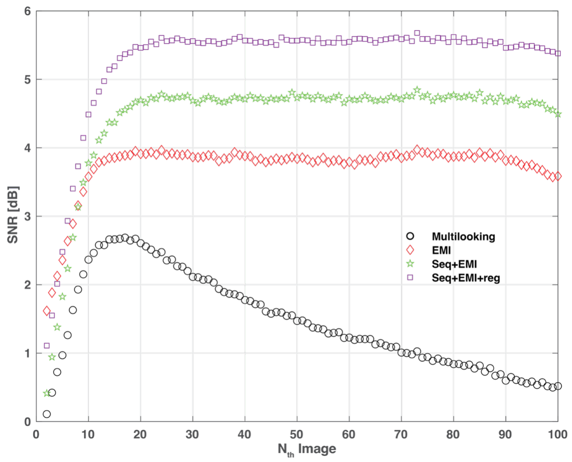

Figure 5. Phase SNR comparison

ized median absolute deviation and an a posteriori coherence threshold greater than 0.35 were applied to mitigate outlier interference. Figure 5 presents the average of the interferograms as the temporal baselines increase. A higher value reflects better phase estimation performance.

Interestingly, the SNR improvement from EMI and Seq+EMI is largely confined to shorter temporal baselines. Unexpectedly, the multilooked phase exhibits negative effects for some longer temporal baseline interferograms, as seen in Figure 5. In comparison, Seq+EMI shows less performance degradation, followed by EMI. The newly proposed method in Figure 5 demonstrates a substantial improvement across all temporal baselines, significantly outperforming other state-of-the-art phase estimation techniques.

3.3 Velocity Results and Error Comparison on Real Data

Figure 6 compares line-of-sight velocity maps estimated using the multilooked phase, EMI, Seq+EMI, and the newly proposed method. In the velocity estimation, we selected only points with temporal coherence higher than 0.5. Across the entire landslide region, the multilooked phase retained 3,049 points, the EMI method retained 17,359 points, and Seq+EMI identified 66,399 points. The newly proposed method detected 87,114 points.

Overall, compared to the previous methods, the new method increased the number of measurement points by approximately 15 times compared to the multilooked phase and by nearly one-third compared to the EMI and Seq+EMI methods. Traditional methods struggled to cover measurement points in mountainous regions, whereas the new method provided a relatively dense distribution of points, even in vegetation-covered areas. This resulted in a substantial increase in observations, with the slow movement of several landslide bodies being delineated more clearly. Notably, the bodies we detected here correspond to velocity contrast boundaries. However, delineating the actual boundaries of landslides requires more detailed geological mapping, and ideally, confirmation of such activity through independent measurements (e.g., GNSS or differential LiDAR).

To validate the accuracy improvement of our proposed method we presented the root mean square errors (RMSE) of the conversion process from unwrapped interferograms to the single reference phase in Figure 7. The higher the RMSE, the lower the accuracy. It can be seen in Figure 7 that our proposed method outperforms the other methods. We also presented the unwrapping cost of all unwrapped interferograms for their unwrapping process after phase reconstruction. If the reconstructed interferograms have higher SNR, the unwrapping cost should be low. In Figure 8, the recorded unwrapping cost of our method is the lowest, and therefore the best performance.

4 Conclusions

Aiming to accurately detect landslide motion in power line regions, we have developed an InSAR phase estimator algorithm that incorporates a novel regularization approach. The proposed method was first validated using synthetic data, demonstrating superior phase recovery performance compared to state-of-the-art techniques. We then applied this method to the Faer landslide region, a high-risk area influenced by both natural and anthropogenic factors. The experimental results confirm the effectiveness of the proposed phase estimator in detecting and characterizing landslide deformation, highlighting its potential for improving geohazard monitoring in challenging environments.

Acknowledgements

We acknowledge Generic Mapping Tools 6.1.0 software (https://www.generic-mapping-tools.org/download/).

Data availability

Sentinel-1 data were freely provided by the European Space Agency (https://scihub.copernicus.eu/).

Funding

The study is supported by the Science and Technology Project of State Grid Corporation of China (Nos. 5200- 5200-202355156A-1-1-ZN).

Conflict of interest

The authors declare no conflict of interest. The funders had no role in the design of the study; in the collection, analyses, or interpretation of data; in the writing of the manuscript; or in the decision to publish the results.

References

Ansari, H., De Zan, F., and Bamler, R. (2017). Sequential Estimator: Toward Efficient InSAR Time Series Analysis. *IEEE Transactions on Geoscience and Remote Sensing*, 55(10):5637–5652, doi:10.1109/tgrs.2017.2711037.

Ansari, H., De Zan, F., and Bamler, R. (2018). Efficient Phase Estimation for Interferogram Stacks. *IEEE Transactions on Geoscience and Remote Sensing*, 56(7):4109–4125, doi:10.1109/tgrs.2018.2826045.

Bateson, L., Cigna, F., Boon, D., and Sowter, A. (2015). The application of the Intermittent SBAS (ISBAS) InSAR method to the South Wales Coalfield, UK. *International Journal of Applied Earth Observation and Geoinformation*, 34:249–257, doi:10.1016/j.jag.2014.08.018.

Berardino, P., Fornaro, G., Lanari, R., and Sansosti, E. (2002). A new algorithm for surface deformation monitoring based on small baseline differential SAR interferograms. *IEEE Transactions on Geoscience and Remote Sensing*, 40(11):2375–2383, doi:10.1109/tgrs.2002.803792.

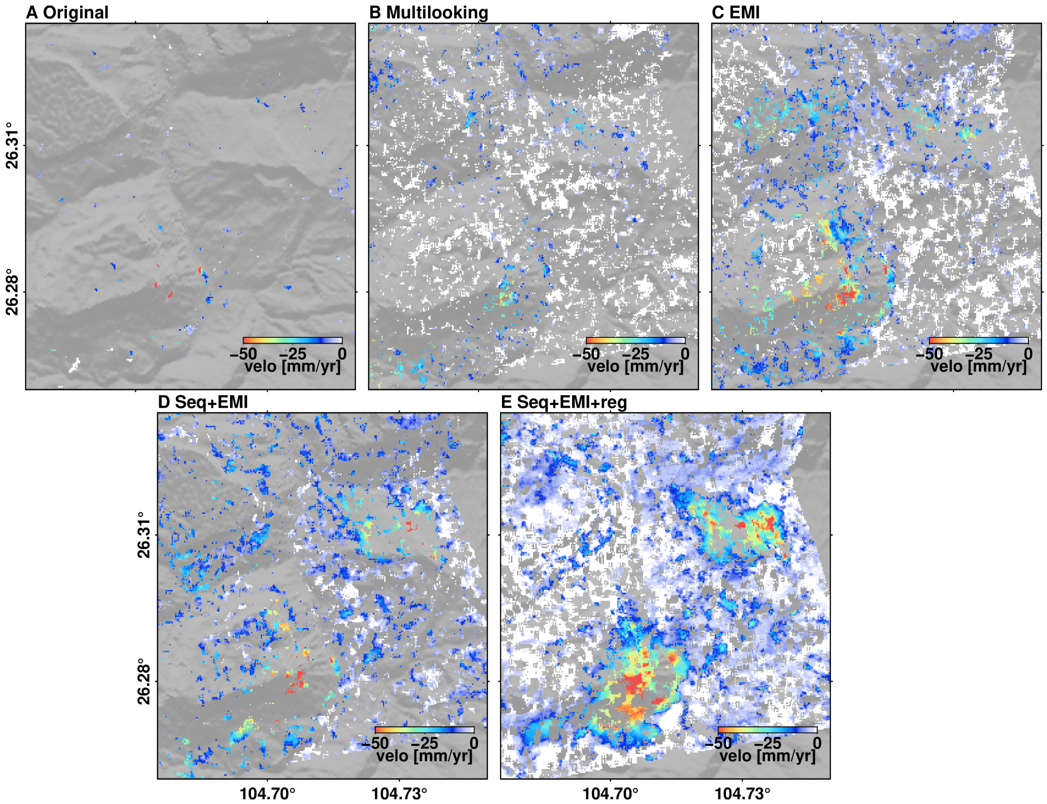

Figure 6. Estimated surface velocity maps (201812044-20230217) from the different methods using InSAR. The velocity maps are all in the ascending track view: (a) original phase, (b) multilooking, (c) EMI, (d) EMI+Seq, and (e) the newly proposed method.

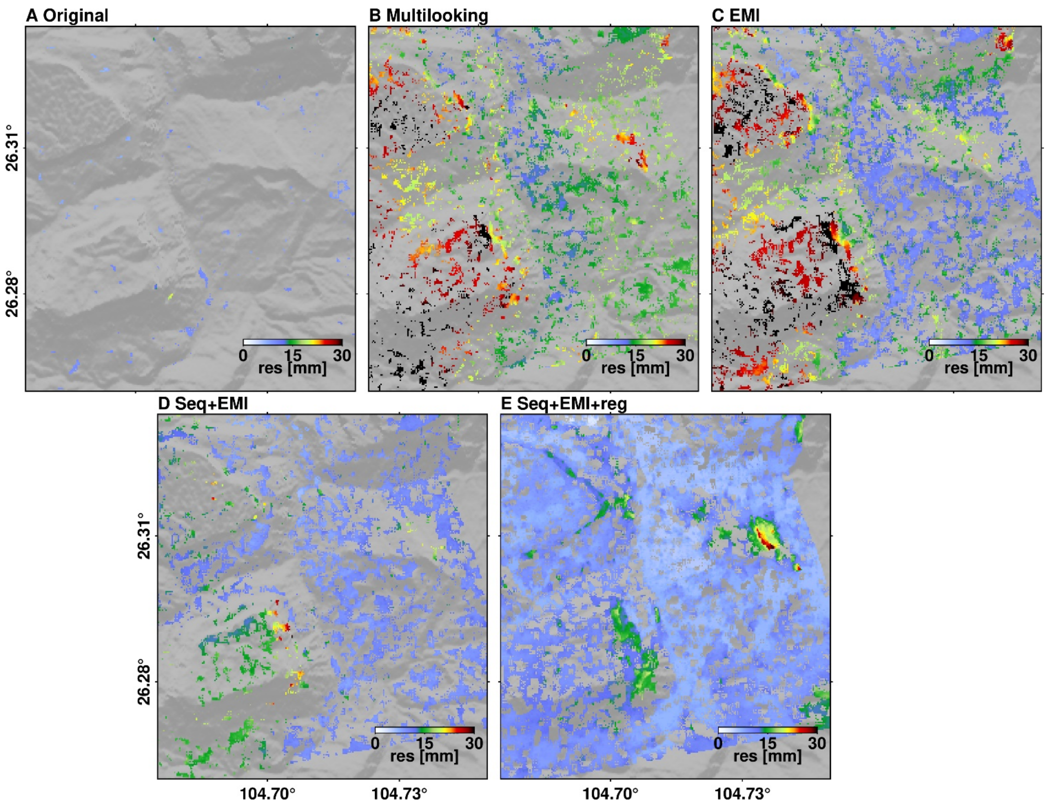

Figure 7. RMSE of the results of the different methods: (a) original phase, (b) multilooking, (c) EMI, (d) EMI+Seq, and (e) the newly proposed method.

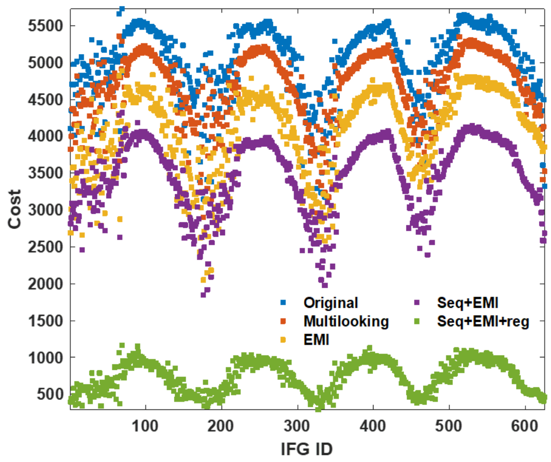

Figure 8. Unwrapping the cost of the different methods for all used SBAS interferograms

Dai, K., Deng, J., Xu, Q., Li, Z., Shi, X., Hancock, C., Wen, N., Zhang, L., and Zhuo, G. (2022). Interpretation and sensitivity analysis of the InSAR line of sight displacements in landslide measurements. *GIScience and Remote Sensing*, 59(1):1226–1242, doi:10.1080/15481603.2022.2100054.

Deledalle, C.-A., Denis, L., Tupin, F., Reigber, A., and Jager, M. (2015). NL-SAR: A Unified Nonlocal Framework for Resolution-Preserving (Pol)(In)SAR Denoising. *IEEE Transactions on Geoscience and Remote Sensing*, 53(4):2021–2038, doi:10.1109/tgrs.2014.2352555.

Dong, J., Qiu, M., Zhao, J., Li, H., and Wu, Q. (2022). Deformation instability mechanism of slope in Fa'er Town, Shuicheng County, Guizhou, China. *Alexandria Engineering Journal*, 61(10):8289–8295, doi:10.1016/j.aej.2022.01.042.

Ferretti, A., Fumagalli, A., Novali, F., Prati, C., Rocca, F., and Rucci, A. (2011). A New Algorithm for Processing Interferometric Data-Stacks: SqueeSAR. *IEEE Transactions on Geoscience and Remote Sensing*, 49(9):3460–3470, doi:10.1109/tgrs.2011.2124465.

Ferretti, A., Prati, C., and Rocca, F. (2001). Permanent scatterers in SAR interferometry. *IEEE Transactions on Geoscience and Remote Sensing*, 39(1):8–20, doi:10.1109/36.898661.

Fobert, M.-A., Singhroy, V., and Spray, J. G. (2021). InSAR Monitoring of Landslide Activity in Dominica. *Remote Sensing*, 13(4):815, doi:10.3390/rs13040815.

Fornaro, G., Verde, S., Reale, D., and Pauciullo, A. (2015). CAESAR: An Approach Based on Covariance Matrix Decomposition to Improve Multibaseline-Multitemporal Interferometric SAR Processing. *IEEE Transactions on Geoscience and Remote Sensing*, 53(4):2050–2065, doi:10.1109/tgrs.2014.2352853.

Guo, J., Cui, Y., Xu, W., Yin, Y., Li, Y., and Jin, W. (2022). Numerical investigation of the landslide-debris flow transformation process considering topographic and entrainment effects: a case study. *Landslides*, 19(4):773–788, doi:10.1007/s10346-021-01791-6.

He, L., Pei, P., Zhang, X., Qi, J., Cai, J., Cao, W., Ding, R., and Mao, Y. (2023a). Sensitivity Evaluation of Time Series InSAR Monitoring Results for Landslide Detection. *Remote Sensing*, 15(15):3906, doi:10.3390/rs15153906.

He, Y., Wang, W., Zhang, L., Chen, Y., Chen, Y., Chen, B., He, X., and Zhao, Z. (2023b). An identification method of potential landslide zones using InSAR data and landslide susceptibility. *Geomatics, Natural Hazards and Risk*, 14(1), doi:10.1080/19475705.2023.2185120.

Hetland, E. A., Musé, P., Simons, M., Lin, Y. N., Agram, P. S., and DiCaprio, C. J. (2012). Multiscale InSAR Time Series (MInTS) analysis of surface deformation. *Journal of Geophysical Research: Solid Earth*, 117(B2), doi:10.1029/2011jb008731.

Hooper, A. (2008). A multi-temporal InSAR method incorporating both persistent scatterer and small baseline approaches. *Geophysical Research Letters*, 35(16), doi:10.1029/2008gl034654.

Hu, K., Wu, C., Tang, J., Pasuto, A., Li, Y., and Yan, S. (2018). New understandings of the June 24th 2017 Xinmo Landslide, Maoxian, Sichuan, China. *Landslides*, 15(12):2465–2474, doi:10.1007/s10346-018-1073-2.

Jia, H., Wang, Y., Ge, D., Deng, Y., and Wang, R. (2022). InSAR Study of Landslides: Early Detection, Three-Dimensional, and Long-Term Surface Displacement Estimation—A Case of Xiaojiang River Basin, China. *Remote Sensing*, 14(7):1759, doi:10.3390/rs14071759.

Jiao, Y.-Y., Wang, Z.-H., Wang, X.-Z., Adoko, A. C., and Yang, Z.-X. (2013). Stability assessment of an ancient landslide crossed by two coal mine tunnels. *Engineering Geology*, 159:36–44, doi:10.1016/j.enggeo.2013.03.021.

Li, W., Zhan, W., Lu, H., Xu, Q., Pei, X., Wang, D., Huang, R., and Ge, D. (2022). Precursors to large rockslides visible on optical remote-sensing images and their implications for landslide early detection. *Landslides*, 20(1):1–12, doi:10.1007/s10346-022-01960-1.

Li, X., Zhou, L., Su, F., and Wu, W. (2021). Application of InSAR technology in landslide hazard: Progress and prospects. *National Remote Sensing Bulletin*, 25(2):614–629, doi:10.11834/jrs.20209297.

Ma, Z.-F., Jiang, M., and Huang, T. (2020). A sequential approach for Sentinel-1 TOPS time-series co-registration over low coherence scenarios. *IEEE Transactions on Geoscience and Remote Sensing*, 59(6):4818–4826, doi:10.1109/TGRS.2020.3009996.

Ma, Z.-F., Jiang, M., Khoshmanesh, M., and Cheng, X. (2021). Time series phase unwrapping based on graph theory and compressed sensing. *IEEE Transactions on Geoscience and Remote Sensing*, 60:1–12, doi:10.1109/TGRS.2021.3066784.

Ma, Z.-F., Jiang, M., Zhao, Y., Malhotra, R., and Yong, B. (2019). Minimum spanning tree co-registration approach for time-series Sentinel-1 TOPS data. *IEEE Journal of Selected Topics in Applied Earth Observations and Remote Sensing*, 12(8):3004–3013, doi:10.1109/JSTARS.2019.2920717.

Moretto, S., Bozzano, F., and Mazzanti, P. (2021). The Role of Satellite InSAR for Landslide Forecasting: Limitations and Openings. *Remote Sensing*, 13(18):3735, doi:10.3390/rs13183735.

Perissin, D. and Wang, T. (2011). Time-Series InSAR Applications Over Urban Areas in China. *IEEE Journal of Selected Topics in Applied Earth Observations and Remote Sensing*, 4(1):92–100, doi:10.1109/jstars.2010.2046883.

Schmitt, M., Schonberger, J. L., and Stilla, U. (2014). Adaptive Covariance Matrix Estimation for Multi-Baseline InSAR Data Stacks. *IEEE Transactions on Geoscience and Remote Sensing*, 52(11):6807–6817, doi:10.1109/tgrs.2014.2303516.

van Natijne, A., Bogaard, T., van Leijen, F., Hanssen, R., and Lindenbergh, R. (2022). World-wide InSAR sensitivity index for landslide deformation tracking. *International Journal of Applied Earth Observation and Geoinformation*, 111:102829, doi:10.1016/j.jag.2022.102829.

Vu, P. V. H., Breloy, A., Brigui, F., Yan, Y., and Ginolhac, G. (2023). Robust Phase Linking in InSAR. *IEEE Transactions on Geoscience and Remote Sensing*, 61:1–11, doi:10.1109/tgrs.2023.3289338.

Wang, Y. and Zhu, X. X. (2016). Robust Estimators for Multipass SAR Interferometry. *IEEE Transactions on Geoscience and Remote Sensing*, 54(2):968–980, doi:10.1109/tgrs.2015.2471303.

Werner, C., Wegmuller, U., Wiesmann, A., and Strozzi, T.

(2003). Interferometric Point Target Analysis with JERS-1 L-band SAR data. In *IGARSS 2003. 2003 IEEE International Geoscience and Remote Sensing Symposium. Proceedings (IEEE Cat. No.03CH37477)*, volume 7 of *IGARSS-03*, pages 4359–4361. IEEE, doi:10.1109/igarss.2003.1295515.

Wu, J. J., Zhi, Q. Q., and Li, X. (2023). Loop source semi-airborne TEM system and its application in landslide detection (in Chinese). *Chinese Journal of Geophysics*, 66(4):1758–1770, doi:10.6038/cjg2022P0960.

Yunjun, Z., Fattahi, H., and Amelung, F. (2019). Small baseline InSAR time series analysis: Unwrapping error correction and noise reduction. *Computers and Geosciences*, 133:104331, doi:10.1016/j.cageo.2019.104331.

Zhang, L., Dai, K., Deng, J., Ge, D., Liang, R., Li, W., and Xu, Q. (2021). Identifying Potential Landslides by Stacking-InSAR in Southwestern China and Its Performance Comparison with SBAS-InSAR. *Remote Sensing*, 13(18):3662, doi:10.3390/rs13183662.

Zhao, C., Dong, Y., Wu, W., Tian, B., Zhou, J., Zhang, P., Gao, S., Yu, Y., and Huang, L. (2023). A Modification to Phase Estimation for Distributed Scatterers in InSAR Data Stacks. *Remote Sensing*, 15(3):613, doi:10.3390/rs15030613.

Zhou, C., Cao, Y., Yin, K., Wang, Y., Shi, X., Catani, F., and Ahmed, B. (2020). Landslide Characterization Applying Sentinel-1 Images and InSAR Technique: The Muyubao Landslide in the Three Gorges Reservoir Area, China. *Remote Sensing*, 12(20):3385, doi:10.3390/rs12203385.